2024 IEEE/RSJ International Conference on Intelligent Robots and Systems (IROS)
October 14-18, 2024. Abu Dhabi, UAE

Passive Underwater Robot Hand Utilizing Water Resistance

Issei Nate and Shinichi Hirai

Abstract— **Numerous robot grippers have been developed to reduce energy consumption by utilizing contact forces with fixed objects. In underwater environments, most objects are not fixed, particularly in the mid and surface layers, posing a challenge for obtaining contact forces. To address this issue, this study proposes a multi-finger gripper that utilizes water resistance for opening and closing actions underwater. As the gripper ascends in water, it closes its fingers, each equipped with a locking mechanism at the tip. This mechanism allows the fingers to maintain a closed shape when converged towards the center and locked. Unlocking occurs when the gripper descends underwater, as the direction of water resistance changes. This design enables locking and unlocking without actuators, offering a solution for grasping underwater objects. The gripper's underwater movement has speed limits. Below the lower limit, fingers may not achieve sufficient bending, while exceeding the upper limit can cause vibrations and affect the locking function. Therefore, maintaining an appropriate speed is crucial. Finally, gripping experiments were conducted to confirm the gripper's ability to grasp objects underwater.**

I. INTRODUCTION

With the proliferation of robotics, various types of grippers have been proposed to serve different purposes. In the development of robot grippers, not only the grasping performance but also the minimization of energy consumption are crucial.

To reduce energy consumption, numerous studies have focused on reducing the number of actuators. One of the representative mechanisms for this purpose is underactuation, which reduces the number of inputs for multiple degrees of freedom. Grippers incorporating this mechanism have been widely proposed [1]–[4]. These grippers can achieve complex movements with fewer actuators.

In addition to reducing the number of actuators, mechanisms have been proposed to minimize the necessary energy consumption by not using actuators to maintain the grasping state. Grippers incorporating deformations of elastic bodies fall into this category [5], [6]. These grippers are designed so that the elastic body exerts a restoring force in the direction of gripper closure, eliminating the need for actuators during closure and thus consuming no energy in the grasping state.

Furthermore, grippers incorporating bistable mechanisms also fall into this category [7]–[11]. These grippers have stable states in both open and closed positions and utilize contact forces with fixed objects to close the gripper. This not only eliminates energy consumption in maintaining the grasping state but also offers advantages such as integration with sensing systems and control techniques, as well as rapid response capabilities.

Moreover, grippers with mechanisms that utilize contact with fixed objects without using actuators at all have also been proposed [12]–[14]. These grippers utilize contact forces or the restoring force of elastic bodies to close the gripper without actuators and open it as well. By incorporating mechanisms that stabilize the gripper in its deformed state, these designs successfully reduce both the number of actuators and the energy consumption required to maintain the grasping state. However, they are limited in environments where contact with flat surfaces or contact forces from fixed objects cannot be obtained, such as underwater surface or mid-layer environments. Especially in industries related to handling aquatic organisms or aquaculture, grippers suitable for these environments are in demand as many aquatic organisms inhabit the mid and surface layers of water bodies.

Various grippers for underwater use have been proposed [15]–[19], expected to be utilized in underwater exploration and aquaculture. These grippers all rely on actuators for opening and closing, and passive mechanisms for opening and closing, as seen in grippers used on land, are not observed.

Therefore, this study proposes a multi-finger gripper capable of opening and closing without actuators underwater by utilizing water resistance. The proposed gripper utilizes the pressure exerted on the fingers during vertical movement underwater. The fingers are designed inspired by the fin ray effect [20]–[22]. Locking mechanisms are attached to the tips of the fingers, and when the tips of the fingers approach each other, the locking mechanism engages, maintaining the bent shape. Unlocking is achieved by utilizing the resistance of water during immersion. This mechanism enables grasping underwater without actuators. Since the fingers are bent by water pressure, they need to be made of extremely soft materials. However, by introducing locking mechanisms, it becomes possible to grasp even heavy objects [23]. Furthermore, conventional grippers intended for underwater use often require various precautions to prevent submersion risks. However, this gripper does not use electrical components, eliminating the need for such precautions, which is a significant advantage.

II. GRIPPER PRINCIPLES

A. Gripper Features

The fingers are shaped by joining two thin plates at their respective lower ends, as illustrated in Fig. 1(a). At the tip, a locking part is attached to enable interlocking between the fingers. A bridge is situated between the two plates to limit

I. Nate and S. Hirai are with Soft Robotics Laboratory, Department of Robotics, Ritsumeikan University, 525-8577 Shiga, Japan. rr0111rv@ed.ritsumei.ac.jp, hirai@se.ritsumei.ac.jp

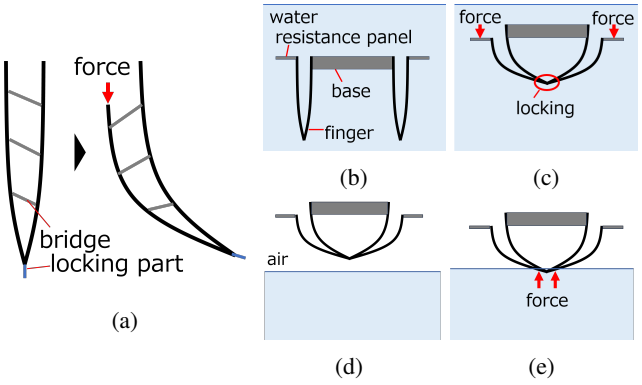

Fig. 1: The drive mechanism of grippers. (a) The mechanism of finger flexion, (b) initial state, (c) ascending underwater, (d) above water, and (e) entry into water in closed state.

the range of motion, allowing the outer plate's upper end to be pressed, causing the finger to bend inward. The upper ends of the inner plates of each finger are fixed to the base, while the upper ends of the outer plates are fixed to the resistance panel.

To operate, the gripper is first moved underwater as shown in Fig. 1(b). Then, as depicted in Fig. 1(c), the gripper is raised from this position. During the ascent, the resistance panel experiences a downward force from the water. Utilizing this force, the fingers bend inward. Each finger is locked by a circular locking mechanism, maintaining the bent shape. In this state, the gripper can grasp the target object, enabling it to be moved above water as shown in Fig. 1(d). To release the lock, the gripper is submerged again as shown in Fig. 1(e). Upon contact with the water, the tips of the fingers experience an upward force, which is used to release the lock, returning the gripper to the state shown in Fig. 1(b).

B. Mechanism for Maintaining Deformed Finger Shape

The circular locking mechanism functions through the interaction of three or more components. All components are evenly arranged around the vertical axis in three-dimensional space, and they move along the axis radially on the horizontal plane. When all components align simultaneously at the center, movement on the horizontal plane is restricted under the condition of equal force applied to all components. However, the components can move in the vertical axis direction. After each component moves in the vertical axis direction and then follows a different path, it returns to the initial state. When all components align at the center, the lock engages. Moving in the vertical axis direction from this state releases the lock.

C. Locking/unlocking Mechnism

The circular locking mechanism employs a locking part as shown in Fig. 2. The locking part consists of flat edge 1, flat edge 2, and a protrusion, and the lock functions through their interference.

Fig. 3 presents a top view and a three-dimensional view of the positional relationship of the locking parts and illustrates

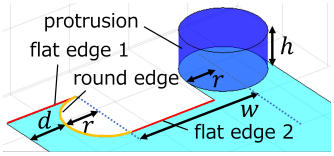

Fig. 2: Names and parameters of locking part.

the principle of locking. The locking part can only exert force in the direction towards and away from the vertical axis on the horizontal plane. Fig. 3(a) shows the initial state. Fig. 3(b) depicts the moment when each locking part moves towards the vertical axis and makes contact with the adjacent locking part at the red point. Fig. 3(c) illustrates the state where the locking part continues to move towards the center while maintaining contact. At this point, each locking part receives a force from the adjacent locking part to the left in the direction of movement, causing them to slightly move to the left and converge towards the center. Fig. 3(d) shows the state where all locking parts are closest. In this state, the forces towards the vertical axis are balanced out due to contact, preventing further movement towards the center. If a force is applied in the direction away from the center in this state, it transitions to the state shown in Fig. 3(e). In this state, the protrusions of each locking part catch onto the round edge of the adjacent locking part, restricting movement away from the center, thus locking the mechanism. In contrast, if the difference in force applied to each locking part becomes significant, the balance of forces will be disrupted, and the lock will cease to function.

The principle of unlocking is illustrated in Fig. 4. Unlocking requires the application of a force in the vertical axis direction. Starting from the state depicted in Fig. 3(e), rotating each locking part around the central axis as shown in Fig. 4(a) removes the contact between the round edge and the protrusion. In this state, movement away from the vertical axis becomes possible again, allowing the mechanism to return to its initial state depicted in Fig. 4(b).

D. Locking Mechanism Design Requirements

To enable the functionality of a lock employing three locking parts, we elucidate the design conditions requisite for its operation and explicate the angular torsion required for unlocking. Two fundamental geometric prerequisites for the proper functioning of the lock are outlined as follows:

(a) In the configuration depicted in Fig. 3(b), it is imperative that the protrusion aligns with flat edge 1.

(b) A state of equilibrium among all applied forces is essential, with the protrusion making contact with flat edge 2.

The first condition, designated as (a), facilitates the receipt of leftward forces by each locking part upon the protrusion's contact with flat edge 1. The geometric relationship at Fig. 3(b) is depicted in Fig. 5(a), and an enlarged view is provided in Fig. 5(b). Defining the centers of all protrusions and round edges on a circle of radius r, denoted as O_1 through O_6, and the center of the contact circle encompassing them as

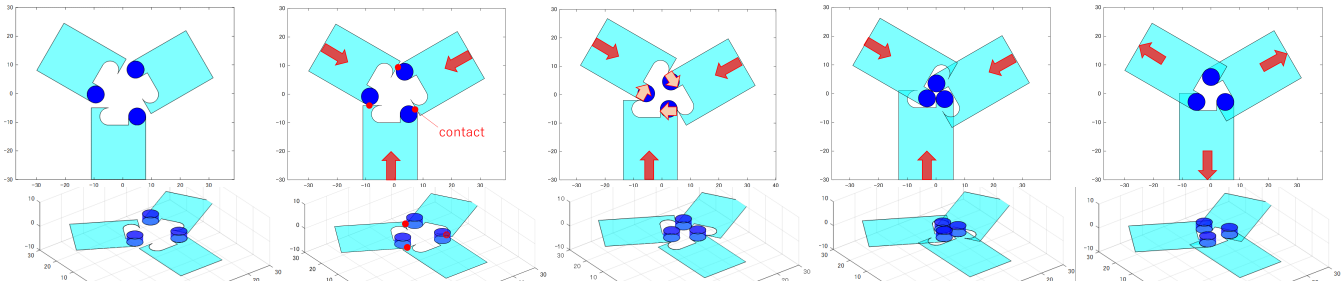

(a) (b) (c) (d) (e)

Fig. 3: Transition Diagram of Locking Mechanism. (a) Initial state, (b) initial contact state of locking part, (c) locking part pushed from right to move left, (d) closest proximity state, and (e) locked state.

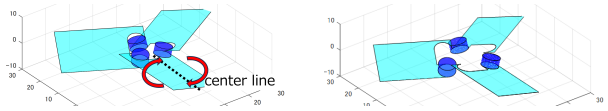

(a) (b)

Fig. 4: Unlocking mechanism. (a) Unlocked position and (b) returning to initial state.

O_0 with a radius of R, we establish that each locking part rotates $2\pi/3$ about O_0. Consequently, the angle θ subtended by $\angle O_1O_0O_3$ equals $2\pi/3$. Due to the symmetry of the locking parts, $O_1O_2 = O_4O_3$, ensuring parallelism between O_2O_3 and O_1O_4 and leading to the equal lengths of O_2P_1 and O_3P_2, both measuring $2r$.

Further, we define O_1P_3 to be the diameter of the contact circle and designate the lengths of segments O_3O_4 and O_4P_3 as m_1 and m_2, respectively. The angle φ, characterized by $\angle O_3O_0O_4$, corresponds to $\pi/3-\varphi$ for $\angle O_4O_0P_3$. Thus, m_1 and m_2 are expressed as:

$$m_1 = 2R\sin\left(\frac{\varphi}{2}\right) \tag{1}$$

$$m_2 = 2R\sin\left(\frac{\pi}{6} - \frac{\varphi}{2}\right) \tag{2}$$

The length of segment O_1O_4, denoted as α, can be derived using the Pythagorean theorem, resulting in $\alpha = \sqrt{(2R)^2 - m_2^2}$. Moreover, given the right triangle $\triangle O_1O_2P_1$ where $O_1P_1 = O_4P_2$, and defining O_4P_2 as m_3, we ascertain:

$$\alpha = 2m_3 + w \tag{3}$$

Subsequently, expressing m_3 as $\sqrt{m_1^2 - (2r)^2}$, we derive the equation for α. Additionally, considering $\theta = 2\pi/3$, the length of segment O_1O_3 equals $\sqrt{3}R$. By the same reasoning, α can be represented as:

$$\alpha = \sqrt{(\sqrt{3}R)^2 - (2r)^2} + m_3 \tag{4}$$

The solution for m_1 can thus be obtained by solving equations (1) through (4).

Furthermore, we identify that when the protrusion and flat edge 1 make contact, the upper end of the round edge P_4 coincides with the contact point P_5, ensuring $P_2O_4 = P_4P_5 = m_3$.

For $w = 10$ and r varying from 0 to 5, we present the values of m_3 and r in Fig. 5(c), where it is evident that m_3 consistently surpasses r.

Thus, in the design, d must satisfy the condition:

$$d > m_3 - r \tag{5}$$

as this constitutes condition (a).

Condition (b) pertains to the necessity for the protrusion to catch onto the round edge when the locking part moves away from the z-axis, starting from a state where the forces in the central direction are balanced, as depicted in Fig. 3(d). To fulfill this condition, it is required that during the transition from the state shown in Fig. 3(c) to that in Fig. 3(d), the protrusion does not make contact with adjacent ones. The geometric configuration satisfying condition (b) is illustrated in Fig. 6(a). Denoting the upper end of the round edge as Q_1 and the intersection point of O_1Q_1 and the circle with center O_1 as Q_2, condition (b) is met when the length of Q_1Q_2 exceeds $2r$. Hence, condition (b) can be expressed as:

$$\sqrt{r^2 + w^2} - r > 2r \tag{6}$$

Failure to satisfy condition (b) results in a state depicted in Fig. 6(b), preventing the transition to the state shown in Fig. 3(d).

Fig. 7 compares the state before and after rotation required for unlocking. Let T_3 denote the left end of the protrusion's upper surface, T_4 the right end of the round edge, and T_5 the foot of the perpendicular from T_4 to the centerline. The angle of rotation of the locking part is denoted as θ_{twist}.

The angle θ_{T_3} between T_3T_5 and the horizontal plane is determined by:

$$\theta_{T_3} = \sin^{-1}\left(\frac{h}{\sqrt{h^2 + \left(\frac{w}{2} + r\right)^2}}\right) - \theta_{twist} \tag{7}$$

Consequently, the height δ_3 of T_3 after rotation is:

$$\delta_3 = \sqrt{h^2 + \left(\frac{w}{2} + r\right)^2}\sin(\theta_{T_3}) \tag{8}$$

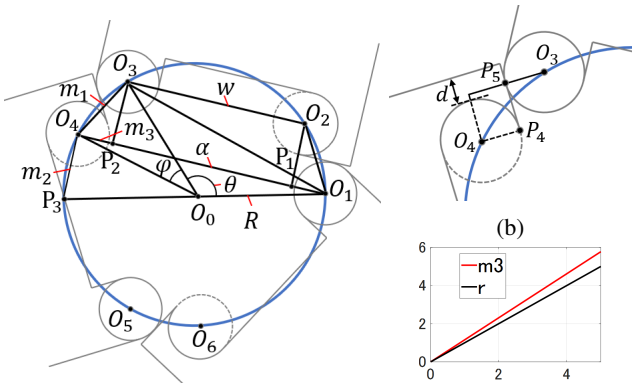

Fig. 5: Geometry meeting condition (a). (a) Top view when locking part contacts adjacent component, (b) detail view, and (c) numerical calculation results

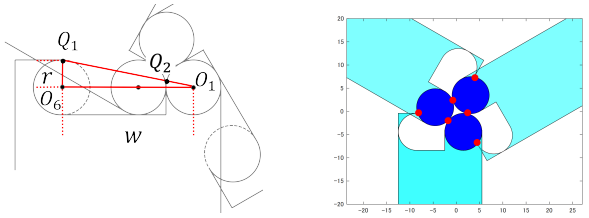

Fig. 6: Geometry meeting condition (b). (a) Top view when locking part is most centralized and (b) state where protrusion is too large to meet condition (b)

Similarly, the height δ_4 of T_4 after rotation is:

$$\delta_4 = \left(\frac{w}{2} + r\right) \sin(\theta_{twist}) \tag{9}$$

The condition necessary for unlocking is that T_4 is positioned above T_3 after rotation. Therefore, unlocking occurs when:

$$\delta_3 < \delta_4 \tag{10}$$

III. Designing the Gripper

A. Finger Deformation Shape Simulation

We constructed a simulation model to predict the deformed shape for determining the shape of the finger. The finger is composed of two plates that deform continuously. The length of each plate is denoted as l, and they are represented

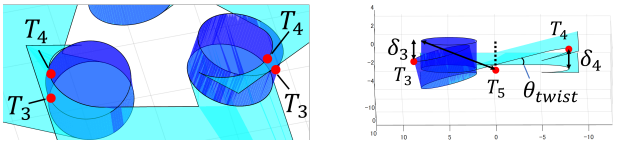

Fig. 7: Diagrams illustrating the target rotation angle required for unlocking. (a) Top view and (b) front view.

by n elastic joints from P_1 to P_n and from $\mathrm{P}_{\mathrm{n}+1}$ to $\mathrm{P}_{2\mathrm{n}-1}$ (Fig. 8(a)). The bending angle of elastic joint P_k is denoted as θ_k. Let P_1 be the origin, with the x-axis pointing horizontally to the right and the y-axis vertically upward. The coordinates of P_k are then given by

$$\begin{bmatrix} x_k \\ y_k \end{bmatrix} = \frac{l}{n} \sum_{j=1}^{k-1} \begin{bmatrix} \sin(\varphi_j) \\ -\cos(\varphi_j) \end{bmatrix} \tag{11}$$

where

$$\varphi_j = \sum_{i=1}^{j} \theta_i \tag{12}$$

The elastic potential energy stored in the joint, denoted as U_J, is expressed as

$$U_J = \frac{1}{2} \frac{\tau^2}{\lambda} \tag{13}$$

where λ is the elastic coefficient of the joint and τ is the torque.

Let E be the Young's modulus of the material, I be the second moment of area of the cross-section, and M be the bending moment. The bending energy U_B when bending a beam of uniform bending stiffness k_b is given by

$$U_B = \frac{1}{2} \frac{M^2 k_b}{EI} \tag{14}$$

Assuming k_b is small with $k_b \simeq l/n$, and $U_J = U_B$, the elastic coefficient R can be approximated as

$$R \simeq \frac{EI}{l} \tag{15}$$

The total potential energy stored in all joints due to deformation is

$$U_F = \sum_{k=1}^{n-1} \frac{1}{2} \lambda \theta_k^2 + \sum_{k=n+1}^{2n-2} \frac{1}{2} \lambda \theta_k^2 \tag{16}$$

The deformation of the finger involves pushing the upper end $\mathrm{P}_{2\mathrm{n}-1} = [\mathrm{x}_{2\mathrm{n}-1}\, \mathrm{y}_{2\mathrm{n}-1}]$ of the outer plate. Therefore, if the displacement distance along the y-axis is s, the constraint for $\mathrm{P}_{2\mathrm{n}-1}$ is

$$y_{2n-1} - s = 0 \tag{17}$$

Furthermore, the distance constraint between two plates is the distance between any two points (Fig. 8(b)). Thus, the constraint is

$$\sqrt{(x_{k1} - x_{k2})^2 + (y_{k1} - y_{k2})^2} - h_b = 0 \tag{18}$$

where h_b is the distance between two points, $\mathrm{P}_{\mathrm{k}1}$, $\mathrm{P}_{\mathrm{k}2}$ are arbitrary points, and defined for the number of bridges used.

The shape of the finger is determined by calculating the θ_k that minimizes U_F. Using the deformation simulation described above, the initial shape of the finger is determined. Initially, the length of the finger is set to $l = 80$ mm, with a width of 16 mm, and the finger is positioned on a circle with a radius of 50 mm. The number of bridges is set to 3. Additionally, the locking part at the tip of the finger is desired to approach horizontally after deformation.

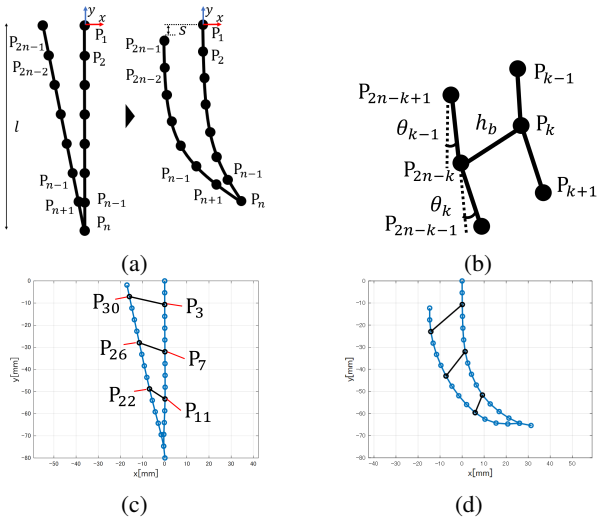

Fig. 8: Simulation model and derived finger shape. (a) Finger composed of two plates represented by multiple joints, (b) enlarged view for representing the distance between two plates, (c) finger with linear shape obtained from simulation, and (d) bent finger.

Thus, $n = 16$, and $\mathrm{P_{k1}\,P_{k2}} = \mathrm{P_3\,P_{30}}, \mathrm{P_7\,P_{26}}, \mathrm{P_{11}\,P_{22}}$. The value of h_b for each bridge is set to prevent plate bending in the initial state: $h_b = 16.3, 12.2, 8.4$. Additionally, to make the tip easier to bend, the thickness at the base is set to 2.4 mm, and at the tip to 0.8 mm, gradually thinning. Consequently, the second moment of area varies from $I = 16 \times 0.8^3/12$ to $16 \times 2.4^3/12$ MPa. The Young's modulus of silicon is set to $E = 1.97$ MPa.

Under these conditions, the shapes generated by the simulation are shown in Fig. 8(c). Fig. 8(d) illustrates the overall finger curvature when P_{2n-1} is pressed inward.

B. Designing the Finger

The finger is required to have very low rigidity because it is deformed by water pressure. Therefore, we used a 3D printer (innovatiQ L320) capable of printing with silicone to create the finger. Fig. 9 shows the finger created based on the simulation. The two plates constituting the finger and the bridges connecting them are integrally molded using the 3D printer.

The locking part created is shown in Fig. 10(a). To reduce water resistance, a design with holes is adopted. The width of the finger is 16 mm, and the thickness varies from 0.8 mm at the thinnest part to 2.4 mm at the thickest part.

At the outer tip of the finger, a twist panel shown in Fig. 10(b) is attached. This allows the finger to utilize the force exerted by water during immersion for twisting action. Resistance panels are shown in Fig. 10(c), with two types created: large panel and small panel. Their respective areas are 14500 mm^2 and 27500 mm^2. The base for securing the finger is shown in Fig. 10(d). The finger with the attached locking part and twist panel is shown in Fig. 11(a). The assembled gripper, consisting of these components, is shown in Fig. 11(b), with three fingers and small panels used for the resistance panels.

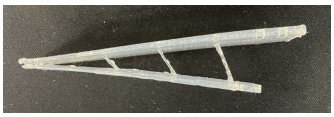

Fig. 9: Silicone finger produced with a 3D printer.

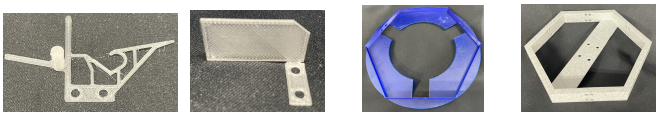

(a) (b) (c) (d)

Fig. 10: Components of the gripper. (a) Locking part, (b) twist panel, (c) resistance panel, and (d) base.

IV. Gripper Speed and Forces Analysis

A. The Mechanism of Finger Flexion

The principle behind the bending of the finger is described as follows. Fig. 12(a) illustrates the positional relationship between the outer and inner parts of the finger when the gripper ascends. The upper end of the inner part of the finger is denoted as T_{in}, and that of the outer part is denoted as T_{out}. As the finger is fixed at the T_{in} section to the base, when the gripper ascends at a constant speed v_g, T_{in} moves at a constant velocity.

At this moment, T_{out} experiences an upward force $f_{(s)}$ due to the ascent of T_{in}, resulting in an upward acceleration a_{out} for T_{out}. The acceleration a_{out} can be expressed by Euler's equation of motion as:

$$a_{out} = \frac{f_{(s)}}{\rho A_r} \tag{19}$$

where A_r represents the area of the resistance plate, and ρ denotes the density of water. Therefore, the relative velocity v_r between T_{in} and T_{out} at time t is given by:

$$v_r = v_g - \int_0^t a_{out}\, dt \tag{20}$$

Additionally, the height difference s between T_{in} and T_{out} is calculated as:

$$s = \int_0^t v_r\, dt \tag{21}$$

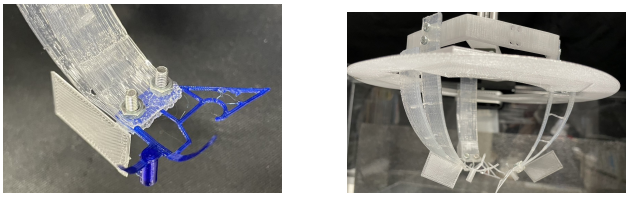

(a) (b)

Fig. 11: Assembly picture. (a) Assembled finger and (b) assembled gripper.

When s exceeds the target value s_t, the finger achieves the desired bending angle.

B. Forces Acting on the Fingers

When an object moves underwater, it experiences resistance from the water. The pressure P_v exerted on a stationary object can be derived from Bernoulli's principle as:

$$P_v = \frac{1}{2}\rho v^2 \tag{22}$$

where v represents the fluid velocity, and ρ is the fluid density. Consequently, the pressure F_v acting on an object with a cross-sectional area A is given by:

$$F_v = \rho v A \tag{23}$$

This expression remains applicable even when the object moves at a velocity v and encounters resistance from the stationary fluid.

Consider the scenario where the gripper ascends at a constant velocity v_g. The forces acting on the finger are illustrated in Fig. 12(b). Considering T_{in} as the origin, the entire finger experiences the force exerted by the water on the resistance panel, denoted as F_1, as well as the forces pushing the inner side of the finger due to the upward movement with velocity v_g, denoted as F_2, and the bending of the finger, denoted as F_3. The forces F_2 and F_3 are considered as the resultant force by aligning the velocity components. Thus, for the entire finger, the "work done by the resistance panel on the finger" is represented as the sum of the "potential energy of the finger" and the "work done by the inner side of the finger on the water". These values are determined using the simulations described in Section 3.

Firstly, the potential energy stored in the finger is given by Equation (16). Next, we determine the work done by the inner side of the finger on the water. The time Δt taken for T_{out} to move Δs in the negative y-direction is expressed as:

$$\Delta t = \frac{\Delta s}{v_r} \tag{24}$$

Let $\boldsymbol{g}_{(s)}$ denote the overall position coordinates of the finger when T_{out} moves s in the negative y-direction. The displacement $\boldsymbol{m}$ of the finger is given by:

$$\boldsymbol{m} = \boldsymbol{g}_{(s)} - \boldsymbol{g}_{(s+\Delta s)} \tag{25}$$

where $\boldsymbol{g}_{(s)}$ represents the vector of all contact point coordinates obtained from the simulations, and any errors in the finger's bending angle due to water resistance are neglected.

Thus, the velocity $\boldsymbol{v}_m$ of all contact points at this moment is given by:

$$\boldsymbol{v}_m = \frac{\boldsymbol{m}}{\Delta t} \tag{26}$$

Since the relative water flow due to the gripper's ascent is downward, each contact point P_k has a velocity component of $v_g \sin(\varphi)$ in the direction of progression, as illustrated in Fig. 12(c). Therefore, the work done by the inner side of the finger on the water is calculated as:

$$U_F = \int_0^{s_t} (\frac{1}{2}\rho \boldsymbol{v}_m^2 lw + \frac{1}{2}\rho v_g \sin\boldsymbol{\varphi}^2 lw) dm \tag{27}$$

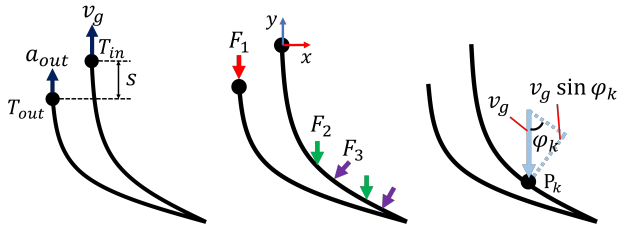

(a) (b) (c)

Fig. 12: Diagram for simulation explanation. (a) Positional relationship between the outside and inside of the finger, (b) relative water flow due to gripper ascent, and (c) force acting on the finger.

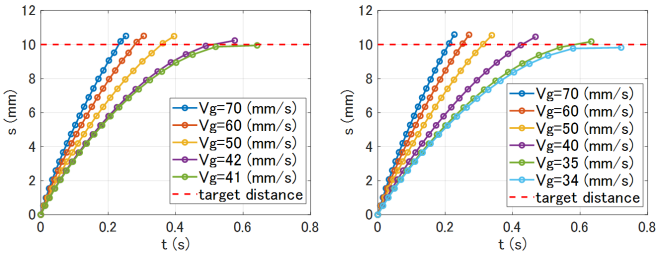

(a) (b)

Fig. 13: Differences in minimum speed due to variations in resistance panel size. (a) Small panel and (b) large panel.

Hence, for the entire finger, the relationship is given by:

$$\int_0^{s_t} f_{(s)} ds = U_p + U_F \tag{28}$$

C. The Relationship Between Robot Movement Speed and Finger Flexion

When the difference between T_{out} and T_{in} exceeds the target distance s_t, the finger achieves the desired bending angle. We aim to determine the conditions that satisfy this criterion.

We conduct analyses for both types of resistance panels. The relationship between the elapsed time and the difference s between T_{out} and T_{in} is presented in Fig. 13. The analysis is terminated when s exceeds the target distance $s_t = 10\,\mathrm{mm}$ or when the increase in s becomes negative. The value of the gripper's ascending velocity v_g is gradually decreased from $v_g = 70\,\mathrm{mm/s}$ until s can no longer exceed the target distance, at which point the analysis is concluded.

From the results, it is observed that there exists a lower limit v_{min} for the gripper's movement speed, below which s does not reach the target value. For the small panel, $v_{\mathrm{min}} = 42\,\mathrm{mm/s}$, and for the large panel, $v_{\mathrm{min}} = 35\,\mathrm{mm/s}$ serve as the lower limits. Furthermore, it is evident that the value of v_{min} decreases as the size of the resistance plate increases.

D. Underwater Driving Experiment

We conducted opening and closing experiments using the actual device, utilizing hydraulic pressure. We recorded the

TABLE I: Experimental results of maximum speed for each resistance panel

	maximum speed [mm/s]	minimum speed [mm/s]
small panel	91	110
large panel	35	78

closing speeds for each of the two types of resistance panels. The results are presented in Table I.

From the experiments, we discovered that there exists not only a lower speed limit but also an upper speed limit. For trials falling below the lower speed limit, after reaching maximum bending angle, the angle decreased. This result aligns with the behavior observed in simulations. However, there was a significant deviation between the calculated and experimental results regarding speed.

In trials where the lock failed due to exceeding the upper speed limit, the fingertip vibrated, resulting in a lack of simultaneous alignment with the gripper's center.

V. Grip Experiment

We conducted grasping experiments underwater, as depicted in Fig. 14(a). The grasped object, with a radius of 25 mm and a height of 15 mm, floated in water (Fig. 14(b)). To keep it in the middle layer of water, a weight of 130 g was attached (Fig. 14(c)). The gripper lifted the object out of the water and released it underwater.

Fig. 15 illustrates the experiment's progress. Submerged underwater, the gripper is shown in Fig. 15(a). Successful locking occurs as the gripper ascends (Fig. 15(b)), followed by successful lifting out of the water (Fig. 15(c)). However, the lock could not be released upon submersion (Fig. 15(d)), as the grasping object continued to exert a load on the fingers.

To examine the lock release mechanism, the grasped object was replaced with a 30 g silicone. Fig. 16 illustrates the scenario when the gripper was submerged. The lock was successfully released upon submersion, and the grasping object was released.

The results indicate that the gripper can grasp objects weighing up to 130 g. For heavier objects, the lock release failed, while it succeeded for lighter objects. This difference is attributed to the density of the grasping object. High-density objects maintain their descent speed upon submersion, continuing to exert a load on the fingers, thus preventing the lock's release. This phenomenon occurs when the object's density significantly exceeds that of water. Conversely, low-density objects experience a decrease in descent speed due to water resistance, creating space between the fingers and reducing the load, allowing the lock to release. This phenomenon is observed with objects having densities close to or less than that of water.

In real environments, high-density objects are unlikely to exist in the upper or middle layers of water in real environments. Therefore, scenarios involving the grasping of high-density objects need not be considered, and the gripper's release performance is deemed sufficient.

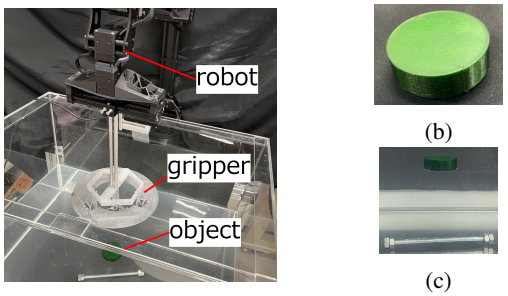

(a) (b) (c)

Fig. 14: Grip experiment setup. (a) Experimental environment, (b) object to be grasped, and (c) state of hanging weights on the grasped object to position it in the middle of the water.

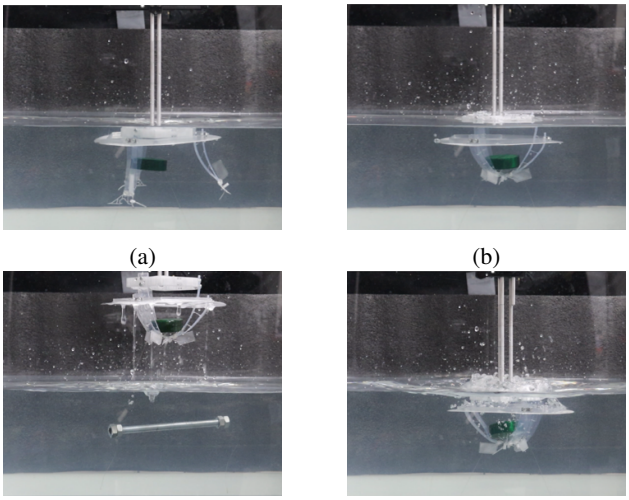

(a) (b) (c) (d)

Fig. 15: Image of gripper grasping an object. (a) Entry into water, (b) the moment of locking, (c) state of lifting the object, and (d) entry into water with failed unlock

VI. CONCLUSIONS

This study proposed a multi-finger robotic gripper capable of grasping objects underwater without using actuators. The gripper utilized water resistance on the fingers when moved up and down underwater to perform opening and closing actions. Each finger was equipped with a locking mechanism, and when all fingers converged at the center of the gripper, the lock engaged, maintaining the bent shape. When the gripper ascended underwater, the fingers locked in place, and the lock was released upon submersion. This mechanism enabled grasping objects without the use of actuators.

Through analysis of the forces acting on the fingers and experimentation, it was determined that an appropriate ascent speed was crucial for closing the gripper and engaging the lock. If the speed was too fast, the fingertips vibrated, preventing the lock from engaging, while if it was too slow, a sufficient bending angle could not be obtained.

In the grasping experiments, it was confirmed that grasping objects underwater was feasible. However, it was also found

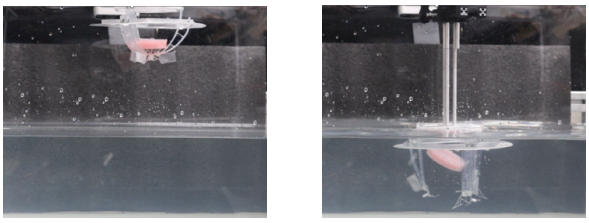

(a) (b)

Fig. 16: Image of experiment with low-density object, focused on unlocking. (a) Gripper in grasping state with object and (b) state of successful unlocking simultaneously with entry into water.

that it was not possible to release the lock when grasping high-density objects.

Since the gripper developed in this study had only three fingers, attempting to grasp a sphere resulted in it rolling out of the gaps and not being gripped. Therefore, future research needs to increase the number of fingers to stabilize grasping accuracy. Additionally, changing the shape of the fingers from plate-like to mesh-like could reduce water resistance.

REFERENCES

[1] Huixu Dong, Ehsan Asadi, Chen Qiu, Jiansheng Dai, and I-Ming Chen. Geometric design optimization of an under-actuated tendon-driven robotic gripper. *Robotics and Computer-Integrated Manufacturing*, 50:80–89, 2018.

[2] Nicolas Rojas, Raymond R Ma, and Aaron M Dollar. The gr2 gripper: An underactuated hand for open-loop in-hand planar manipulation. *IEEE Transactions on Robotics*, 32(3):763–770, 2016.

[3] Xiaodong Zhou, Qiang Zhang, Jianfeng Li, and Yuan Kong. Design of a novel parallel and self-adaptive under-actuated robotic hand. In *2020 IEEE International Conference on Advances in Electrical Engineering and Computer Applications(AEECA)*, pages 859–862, 2020.

[4] Alireza Ahrary. A novel approach to mechanical design of under-actuated robot finger. In *2012 IEEE International Conference on Control System, Computing and Engineering*, pages 286–289, 2012.

[5] Mingjun Li, Manjia Su, Rongzhen Xie, Yihong Zhang, Haifei Zhu, Tao Zhang, and Yisheng Guan. Development of a bio-inspired soft gripper with claws. In *2017 IEEE International Conference on Robotics and Biomimetics (ROBIO)*, pages 828–833, 2017.

[6] Kenji Nagaoka, Hayato Minote, Kyohei Maruya, Yuki Shirai, Kazuya Yoshida, Takeshi Hakamada, Hirotaka Sawada, and Takashi Kubota. Passive spine gripper for free-climbing robot in extreme terrain. *IEEE Robotics and Automation Letters*, 3(3):1765–1770, 2018.

[7] Ryan L Harne and KW Wang. A review of the recent research on vibration energy harvesting via bistable systems. *Smart materials and structures*, 22(2):023001, 2013.

[8] Haijie Zhang, Elisha Lerner, Bo Cheng, and Jianguo Zhao. Compliant bistable grippers enable passive perching for micro aerial vehicles. *IEEE/ASME Transactions on Mechatronics*, 26(5):2316–2326, 2021.

[9] Thomas George Thuruthel, Syed Haider Abidi, Matteo Cianchetti, Cecilia Laschi, and Egidio Falotico. A bistable soft gripper with mechanically embedded sensing and actuation for fast grasping. In *2020 29th IEEE International Conference on Robot and Human Interactive Communication (RO-MAN)*, pages 1049–1054, 2020.

[10] HaoTse Hsiao, Feiyu Wu, Jiefeng Sun, and Jianguo Zhao. A novel passive mechanism for flying robots to perch onto surfaces. In *2022 International Conference on Robotics and Automation (ICRA)*, pages 1183–1189, 2022.

[11] Huixu Dong, Chao-Yu Chen, Chen Qiu, Chen-Hua Yeow, and Haoyong Yu. Gsg: A granary-shaped soft gripper with mechanical sensing via snap-through structure. *IEEE Robotics and Automation Letters*, 7(4):9421–9428, 2022.

[12] Issei Nate, Zhongkui Wang, and Shinichi Hirai. Passive robotic gripper using a contact-based locking mechanism. In *2023 IEEE International Conference on Robotics and Automation (ICRA)*, pages 10303–10309, 2023.

[13] Issei Nate, Zhongkui Wang, and Shinichi Hirai. Origami-based robotic gripper for transporting solids with liquids. In *2024 IEEE/SICE International Symposium on System Integration (SII)*, pages 251–256. IEEE, 2024.

[14] Jessica McWilliams, Yifan Yuan, Jason Friedman, and Cynthia Sung. Push-on push-off: A compliant bistable gripper with mechanical sensing and actuation. In *2021 IEEE 4th International Conference on Soft Robotics (RoboSoft)*, pages 622–629, 2021.

[15] Nina R Sinatra, Clark B Teeple, Daniel M Vogt, Kevin Kit Parker, David F Gruber, and Robert J Wood. Ultragentle manipulation of delicate structures using a soft robotic gripper. *Science Robotics*, 4(33):eaax5425, 2019.

[16] Hannah Stuart, Shiquan Wang, Oussama Khatib, and Mark R Cutkosky. The ocean one hands: An adaptive design for robust marine manipulation. *The International Journal of Robotics Research*, 36(2):150–166, 2017.

[17] Kevin C Galloway, Kaitlyn P Becker, Brennan Phillips, Jordan Kirby, Stephen Licht, Dan Tchernov, Robert J Wood, and David F Gruber. Soft robotic grippers for biological sampling on deep reefs. *Soft robotics*, 3(1):23–33, 2016.

[18] Daniel M Vogt, Kaitlyn P Becker, Brennan T Phillips, Moritz A Graule, Randi D Rotjan, Timothy M Shank, Erik E Cordes, Robert J Wood, and David F Gruber. Shipboard design and fabrication of custom 3d-printed soft robotic manipulators for the investigation of delicate deep-sea organisms. *PloS one*, 13(8):e0200386, 2018.

[19] Zhi Ern Teoh, Brennan T Phillips, Kaitlyn P Becker, Griffin Whittredge, James C Weaver, Chuck Hoberman, David F Gruber, and Robert J Wood. Rotary-actuated folding polyhedrons for midwater investigation of delicate marine organisms. *Science Robotics*, 3(20):eaat5276, 2018.

[20] Whitney Crooks, Gabrielle Vukasin, Maeve O ' Sullivan, William Messner, and Chris Rogers. Fin ray® effect inspired soft robotic gripper: From the robosoft grand challenge toward optimization. *Frontiers in Robotics and AI*, 3:70, 2016.

[21] C. I. Basson, G. Bright, and A. J. Walker. Validating object conformity through geometric considerations of gripper mechanisms. In *2017 24th International Conference on Mechatronics and Machine Vision in Practice (M2VIP)*, pages 1–6, 2017.

[22] Whitney Crooks, Shane Rozen-Levy, Barry Trimmer, Chris Rogers, and William Messner. Passive gripper inspired by manduca sexta and the fin ray® effect. *International Journal of Advanced Robotic Systems*, 14(4):1729881417721155, 2017.

[23] Xin-Yu Guo, Wen-Bo Li, Qiu-Hua Gao, Han Yan, Yan-Qiong Fei, and Wen-Ming Zhang. Self-locking mechanism for variable stiffness rigid–soft gripper. *Smart Materials and Structures*, 29(3):035033, 2020.